

(Invited) The Interplay of Conformation and Electronic Structure in Metal Organic Frameworks

The Interplay of Conformation and Electronic Structure in Metal Organic Frameworks

Y. Pramudya^a, M. Kozłowska^a, S. Heidrich^a, M. Krstić^b, R. Haldar^c, T. Neumann^d, T. Schloeder^a, Q. Zhang^c, F. Symalla^d, Z. M. Hassan^b, and X. Liu^c, L. Heinke^c, and C. Woll^c
W. Wenzel^a

^aKarlsruhe Institute of Technology, Institute of Nanotechnology, Hermann-von-Helmholtz Platz-1, 76344 Eggenstein-Leopoldshafen, Germany

^bKarlsruhe Institute of Technology, Institute of Theoretical Solid State Physics (TFP), Wolfgang-Gaede-Str. 1, 76131 Karlsruhe, Germany

^cKarlsruhe Institute of Technology, Institute of Functional Interfaces, Hermann-von-Helmholtz Platz-1, 76344 Eggenstein-Leopoldshafen, Germany

^dNanomatch, Griesbachstr. 5, 76185, Karlsruhe, Germany

Metal organic frameworks (MOFs) are a fascinating class of materials that is currently investigated in the context of many applications. The large size of the chemical space of these systems, comprising organic linkers connected by metal centers, precludes an exhaustive experimental search for optimal materials. For this reason, a variety of modeling tools, ranging from structure-generators to electronic structure methods has been applied to understand and increasingly predict their function. Here we review some recent studies, where computational methods were used to elucidate MOF properties, such as electroluminescence, refraction index, and charge transports. As these methods become more predictive, they enable computational screening of MOF materials.

Introduction

The emergence of metal organic frameworks (MOFs)¹ as a new class of porous materials has an enormous potential for diverse applications such as: gas storage/sorption², molecular separation³, insulation, catalysis, optics, and light sensitive semiconducting properties while maintaining its porosity.⁴⁻⁶ MOFs building blocks consist of metal nodes or secondary building units (SBU), and organic ligands/linkers with end groups that can covalently bond with metals such as carboxylates. Highly ordered thin film structures of surface-anchored metal organic framework (SURMOF) open wide applications based on more than just the porosity-related properties of MOFs. To study the electronic properties (electroluminescence, refraction index, and charge transports) of MOFs and SURMOFs, multi-scale approaches are required.

A wide variety of computational tools has been established over the years to facilitate the modeling of MOFs: as the first step, molecular models are often generated from X-ray diffraction data (XRD), or with MOF builder tools such as AuToGraFS⁷. The geometry and structural properties can then be modeled with classical force fields, in particular when XRD data are not available. Such classical force fields have been used extensively in biology and organic materials but often struggle to describe the structural

properties of MOFs because the metal to organic bonds at the MOF nodes are not well parametrized in most force fields. Semiempirical methods such as density functional tight binding (DFTB) have also been used, but did not give significant improvement over classical force field methods such as UFF or UFF4MOF.^{8,9,10} Application of DFTB methods in modeling of MOFs has been limited by the small number of parametrized metals (Zn, Al, Au, Si, and alkaline earth) and their organic complexes due to the complexity of parametrization.¹¹ Recent generations of tight-binding methods such as GFN2-xTB are able to deal with almost the entire range of elements in the periodic table, but have not been tested widely in MOF applications.¹²

Electronic properties of MOFs are typically studied using quantum mechanical (QM) methods. The most popular method is Density Functional Theory (DFT), which due to its versatility has been widely used to calculate the ground states of periodic models and cluster molecular models of MOFs. To study excited state electronic properties, such as light absorption/emission spectra and refractive indices, one can employ the Time-Dependent Density Functional Theory (TD-DFT) method, the Random Phase Approximation (RPA), or the parametrization-free (for correlation and exchange) Green's Function (GW) and Bethe-Salpeter Equation (BSE) methods. However, the GW+BSE method is extremely demanding in terms of computational effort and can presently not be applied to large MOF structures, either for ground or excited state geometry optimization.^{13,14} As an alternative, TD-DFT methods in molecular cluster models can be used to approximately describe the electronic properties (absorption/emission) of electronically excited states. For refractive index calculations, a method to determine the ground and excited state properties using the random phase approximation (RPA)¹⁵⁻¹⁷ in TD-DFT using a molecular model was shown to be sufficient.

Because most MOFs have very flat conduction and valence bands (heavy bare electron/hole effective mass),¹⁸ charge transport is often well-approximated by hopping transport¹⁹ models, but sometimes band-like transport is also considered.²⁰ In the following, we review conductivity calculations using specially adapted quantum embedding methods such as Quantum Patch^{21,22} to model the electronic structure. Using input from these calculations, Kinetic Monte Carlo (KMC) methods, such as LightForge KMC²³ can be used to describe transport on larger scales.

In this proceeding, we review examples of challenging problems to model the electronic structure of MOFs, such as:

1. A de novo Strategy for Predictive Crystal Engineering to Tune Excitonic Couplings;⁶
2. Light-Switchable One-Dimensional Photonic Crystals Based on MOFs with Photomodulatable Refractive Index;²⁴
3. Highly Efficient One-Dimensional Triplet Exciton Transport in a Palladium–Porphyrin-Based Surface-Anchored Metal–Organic Framework;²⁵
4. Photoconductivity in Metal–Organic Framework (MOF) Thin Films;⁵ and
5. Superexchange Charge Transport in Loaded Metal Organic Frameworks.²⁶

In the discussion of these problems we also briefly review the implementations of the required computational methods from classical molecular dynamics (MD) to the quantum level (DFT, RPA).

1. A de novo Strategy for Predictive Crystal Engineering to Tune Excitonic Couplings⁶

In the first example, we developed a multi-scale screening strategy to suppress undesirable photoluminescence (PL) quenching by optimizing chromophore packing and systematically changing side-groups of the organic linkers which worked as “steric control units” (SCUs). The nonradiative decay processes caused by excitonic coupling to adjacent chromophores could be reduced and the PL signal was increased by substituting the adjustable SCUs. Furthermore, we found optimal alignment of core-substituted naphthalenediimides (cNDIs) to obtain highly emissive J-aggregates using computational analysis. The schematic of the workflow is shown in Fig. 1.

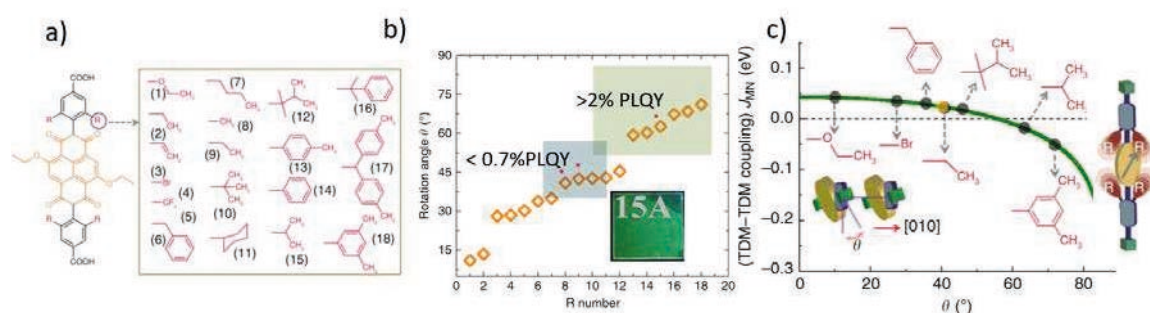


Figure 1. a) Chemical structure of R-NDI(OEt)₂ with possible R groups. b) Rotational angles from MD simulations vs different R groups from Fig. 1a) resulted in a region with borderline blue emission and J-aggregates with bright green emission within synthesized SURMOF structures marked with red stars. The inset in the bottom right corner shows a microscope image of highly J-aggregated emission of the SURMOF. c) Calculated Coulomb coupling between two optically active parts of neighboring NDI organic linkers within the SURMOF structure. The transition dipole moments (TDM) coupling simulated from transition charges using the electrostatic potential method (TrEsp) vs rotational angles predicted by MD in GROMACS-2018.4. The yellow ellipsoid represents the NDI(OEt)₂ with the transition dipole vector orientation shown as a grey arrow.⁶

The multi-scale approach consisted of the following steps: 1. We created a library of chromophoric MOF linkers with suitable contact groups and computationally screened for the best SCUs by obtaining the optimized geometry of the R-functionalized bis-ethoxy substitute-naphthalenediimides, dubbed R-NDI(OEt)₂ monomer (Fig. 1a)), with the OPLS force field. We used this approach to tune the optimum layer distance between 2D sheets of SURMOF (5-8 Å, with 5.8-6.0 Å being the minimum), and extracted the optimal rotation angle of the central linker from the geometry (Fig. 1b)). 2. We then built trimer models of MD-optimized linkers with fixed intermolecular distances and re-optimized the middle linker using full gradient minimization techniques in DFT. 3. The middle linker from the DFT optimization was used to build a dimer model to study the angle-dependent Coulomb coupling using the electrostatic potential method (TrEsp, Fig. 1c)), which takes into account the influence of different SCUs and NDI(OEt)₂ alignment in the SURMOF, with TD-DFT using the B3LYP functional, Grimme D3 van der Waals correction with Becke-Johnson damping and the def2-TZVP atomic orbital basis set. The results, shown in Fig. 1c), predicted highly emissive J-aggregates (R=iPr, no. 15 in Fig. 1b)), which was confirmed by experiments. Optimized predicted structures showed an increase of more

than 2% in photoluminescence quantum yields (PLQY) compared to other experimentally tested compounds, e.g. compounds 8, R=Me, and 9, R=Et in Fig. 1b). The prediction based on computational screening is in excellent agreement with experimental findings and 2% PLQY is the highest ever recorded quantum yield for crystalline materials based on naphthalenediimides.

2. Light-Switchable One-Dimensional Photonic Crystals Based on MOFs with Photomodulatable Refractive Index²⁴

As a second example we review the optical properties of light-switchable 1D photonic SURMOF crystals. Photomodulation of the refractive index is facilitated via reversible light-induced trans-cis isomerization of the linkers. We calculated the properties of the two linker isomers (cis and trans azobenzene) using the random phase approximation (RPA) based on TD-DFT electronic structure calculations. The resulting index of refraction was directly compared to experimental data (Fig. 2a)). The transition density of the $\pi - \pi^*$ interaction is shown in Fig. 2b) for trans and cis isomers of the linker molecules.

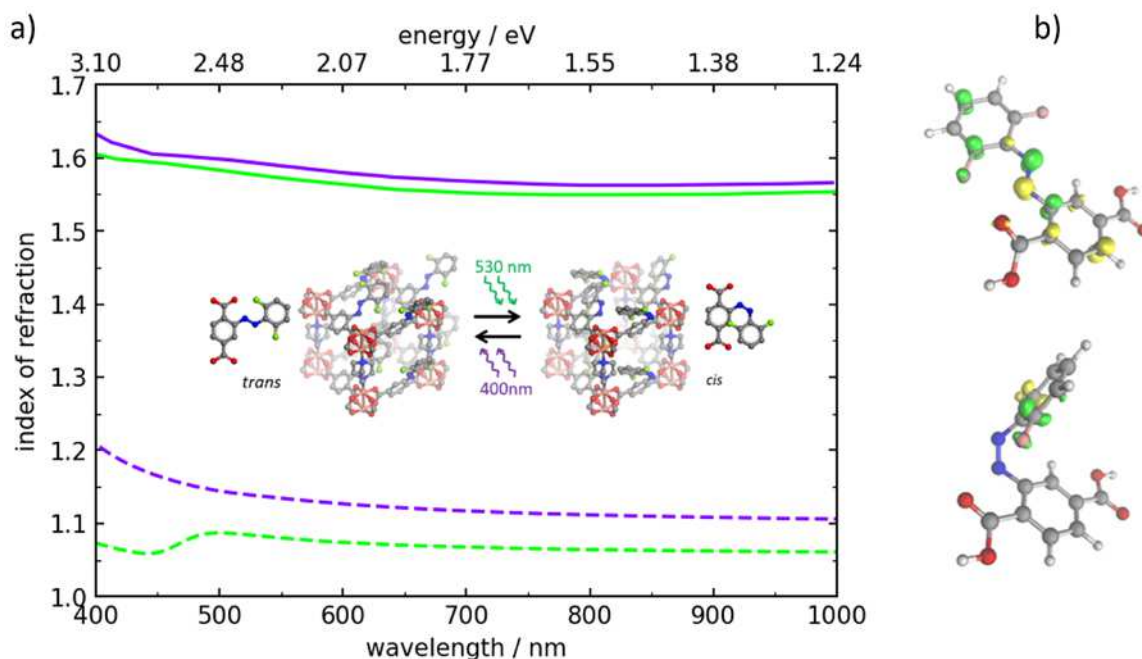


Figure 2. a) Refractive index of cis (green) and trans (violet) linker configurations from experiment (solid lines) and theory (dashed lines), where the latter neglects the rest of the MOF structure. b) Singlet excited state transition density for the $\pi - \pi^*$ transition, with negative and positive phases shown in yellow and green, respectively.²⁴ Reprinted with permission from Ref. 24. Copyright 2019 American Chemical Society.

We note that only qualitative agreement can be achieved, because RPA neglects exchange-correlation effects in the excited response. To obtain quantitatively accurate results for excited states and therefore optical properties, more costly methods, such as the Bethe-Salpeter Equation (BSE) approach would be required.

3. Highly Efficient One-Dimensional Triplet Exciton Transport in a Palladium–Porphyrin-Based Surface-Anchored Metal–Organic Framework;²⁵

As a third example we discuss the analysis of triplet exciton transport in a Palladium-Porphyrin (PdP) based SURMOF using TD-DFT. The periodic structure of the SURMOF is shown in Fig. 3a). It was a tetragonal SURMOF structure bonded with a Zn-paddlewheel SBU/node. The $\pi - \pi^*$ interaction in PdP linkers are visualized as intermolecular noncovalent interactions (NCI) shown in yellow in Fig. 3b). The ground and triplet excited states of the PdP dimer were calculated with TD-DFT using the CAM-B3LYP functional. The electron donating and accepting regions (through Dexter transfer between linkers) of the dimer model are marked in violet and green in Figure 3c). The calculated rate of triplet excited exciton transfer (TEET) was $1.01 \times 10^{10} \text{ s}^{-1}$, which was nearly of the same order of magnitude as that from the experimental data at $8.00 \times 10^{10} \text{ s}^{-1}$. The theoretical TEET rates were highly dependent on the functional used in TD-DFT. For instance, the TEET rate found with B3LYP functional was $0.6 \times 10^{10} \text{ s}^{-1}$, which was half of the value obtained using CAM-B3LYP.

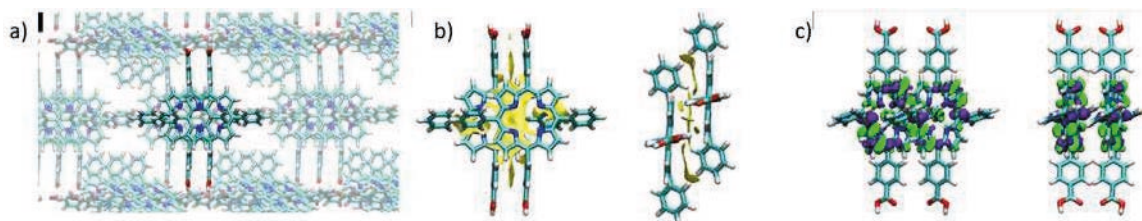


Figure 3. a) Periodic structure of the palladium-porphyrin MOF, b) $\pi - \pi^*$ interaction, and c) electron density difference between ground state and triplet excited state of the PdP dimer.²⁵ Reprinted with permission from Ref. 25. Copyright 2019 American Chemical Society.

4. Photoconductivity in Metal–Organic Framework (MOF) Thin Films⁵

The fourth example was the photoactivated electronic transport phenomenon in a porphyrin SURMOF loaded with C_{60} . TD-DFT was used to elucidate the possible origin of remarkable photoconduction; the electrical conductivity increased by 2 orders of magnitude when irradiated with visible light with a wavelength of 455nm (2.72 eV). We believed the process started with porphyrin moieties absorbing the light, followed by C_{60} accommodating rapid charge separation due to its large electron affinity. Subsequently, electronic transport through separate channels formed by porphyrin for holes and C_{60} for electrons resulted in high conductivity. Loading of C_{60} inside the SURMOF had been confirmed by XRD, UV/Vis absorption, and IR measurements.

In this study, the nature of light-activated conductivity was studied theoretically. Fig. 4a) shows the building blocks of the SURMOF, and Fig. 4b) the optimized geometry of the SURMOF structure from periodic DFT calculations using the PBE functional and D3 Van der Waals correction as implemented in Vienna Ab-initio Simulation Package (VASP 5.4.4). With loaded C_{60} in the SURMOF, the conductivity exhibited ohmic behavior upon irradiation with light. Experimental findings showed $\sigma_{ohmic} \sim$

$1.3 \times 10^{-7} \text{ S m}^{-1}$, which is two orders of magnitude higher than the activated-like (hard-gap) conductivity $\sigma_{hard-gap} \sim 1.5 \times 10^{-9} \text{ S m}^{-1}$ in the dark.

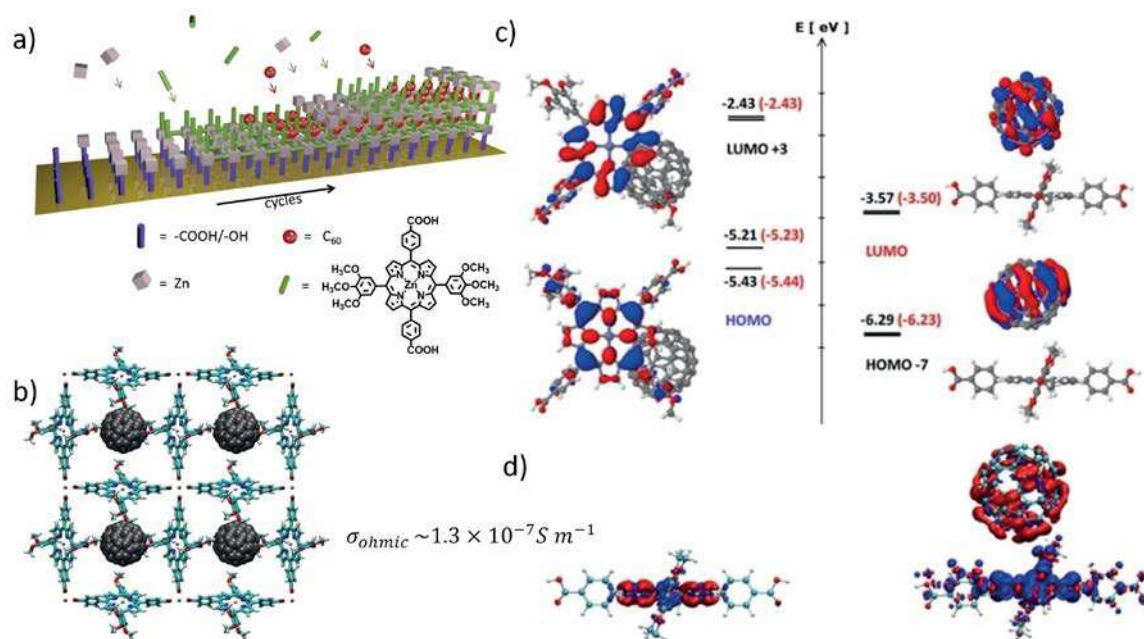


Figure 4. a) SURMOF assembly, b) structure of $C_{60}@Zn(TPPP)$, c) HOMO and LUMO orbitals of the electron acceptor (TPP linker) and donor (C_{60}) and corresponding orbital energies. The energies of TPP- C_{60} complex are printed in black and the energies of isolated TPP and C_{60} are printed in red. d) The singlet-singlet excitation electron density with and without C_{60} near the TPP linker.⁵ Reprinted with permission from Ref. 5, Copyright 2019 John Wiley and Sons.

Investigation of the mechanism of charge transport in $C_{60}@Zn(TPP)$, a loaded SURMOF with C_{60} , was carried out using our in-house Quantum Patch method for calculating the electronic coupling matrix elements between MOF linkers and C_{60} . The results were based on molecular orbitals estimated using DFT. We used the molecular/cluster system of the TPP linker and C_{60} . Fig. 4c) shows the highest occupied molecular orbitals (HOMOs) and lowest unoccupied molecular orbitals (LUMOs) and associated energy levels of pristine Zn(TPP) linker (left) and pristine C_{60} (right). HOMO-7 and LUMO+3 labels corresponded to the orbitals of the Zn(TPP)- C_{60} complex. Comparison between the singlet-singlet excitation electron density of pristine porphyrin (left) and porphyrin in the Zn(TPP)- C_{60} complex showed the electron donation from TPP to C_{60} (Fig. 4d)).

5. Superexchange Charge Transport in Loaded Metal Organic Frameworks²⁶

The last example were the electronic transport properties of HKUST-1 SURMOF loaded with 7,7,8,8-tetracyanoquinodimethane (TCNQ) and its fluorinated compound F4-TCNQ, published in ACS Nano, 2016.²⁶ HKUST-1/MOF-199 is a popular MOF made out of Zn-paddlewheel secondary building units (SBU) and benzene-1,3,5-tricarboxylate (BTC)

linkers. Within the Marcus theory of charge transfer, the rate of hopping events between two sites a and b along a path is described by

$$\Gamma_{a,b} = \frac{2\pi}{\hbar} |J_{a,b}|^2 \sqrt{\frac{1}{4\pi k_B T \lambda}} \exp\left(-\frac{(\lambda + \Delta E_{a,b})^2}{4\lambda k_B T}\right). \quad (1)$$

$J_{a,b}$ is the electronic coupling matrix element between initial state a and final state b , $E_{a,b}$ is the difference between energy levels of the relevant molecular orbitals, and λ is the reorganization energy. The rest are physical constants and parameters: k_B , T , and \hbar are Boltzmann constant, temperature, and Planck constant, respectively. The occupied and unoccupied orbitals of molecular fragments of TCNQ@HKUST-1 and F4-TCNQ@HKUST-1 were calculated using DFT as implemented in TURBOMOLE using the BH-LYP functional and dev2-SV(P) basis set, and the hopping matrix elements J were calculated using Löwdin orthogonalization.¹⁹ These hopping processes are illustrated in Fig. 5a) and b).

In the lowest-energy configuration, the computed coupling matrix elements of the relevant combinations of LUMO orbitals in direct guest-guest hopping between TCNQ molecules are 1.7×10^{-8} eV for parallel and 4.1×10^{-8} eV for orthogonal orientations, and these numbers were comparable to those for F4-TCNQ. In both guests, these coupling matrix elements were much smaller than guest-host (MOF) and host-host couplings. The guest-host coupling for TCNQ was 1.4×10^{-3} eV, which is of the same order of magnitude as that for F4-TCNQ at 2.4×10^{-3} eV. The reorganization energies, λ , calculated with Nelsen's four-point method for all relevant hopping sites for guest molecules were ~ 0.27 eV for TCNQ and F4-TCNQ, and ~ 0.58 eV for MOF fragments. In the guest-guest hopping only scenario, the activation energy would be 67 meV, which agreed with the activation energy observed in experiments. However, the activation energy of hopping processes involving MOF states was much higher.

As a second scenario, second-order processes, or superexchange charge transfers, were considered in addition to direct hops. In superexchange charge transfer processes, the total coupling matrix element between two guest molecules g and g' is determined by the coupling between the initial and intermediate host states J_{gh}^{dir} , and between the intermediate and the final guest states $J_{hg'}^{dir}$ via first order perturbation theory, stated as:

$$J_{gg'}^{tot} = J_{gg'}^{dir} + J_{gg'}^{sx} = J_{gg'}^{dir} + \sum_h \frac{J_{gh}^{dir} \times J_{hg'}^{dir}}{\Delta E_{sx} + \frac{1}{2}\lambda}, \quad (2)$$

where $J_{gg'}^{dir}$ is the direct electronic coupling matrix element, $J_{gg'}^{sx}$ is the coupling matrix element of superexchange processes, and h is the virtually occupied intermediate host state. The denominator $\Delta E_{sx} = E_h - \frac{1}{2}(E_g + E_{g'})$ is due to the fact that occupation of the virtual states is too short to allow for ionic relaxation. It is worth mentioning that the calculation of HOMO-LUMO gaps for the relatively large MOF fragments, and results from hybrid TD-DFT had been shown to strongly depend on the exchange functional used and were computationally demanding. Therefore, the calculation of the energy differences ΔE_{gh} , ΔE_{sx} had large method-dependent uncertainties; thus, they were treated as free parameters. If the estimated $\Delta E_{gh} > 0.4$ eV for both guest molecules, the competing direct

process activation energy became $E_a = \frac{\lambda}{4} (1 + \Delta E_{gh} / \lambda)^2 > 0.41 \text{ eV}$. This activation energy was one order of magnitude greater than the experimental observations (present value 0.041 eV).²⁷ In the pristine MOF, $E_a \sim \lambda/4 = 0.145 \text{ eV}$ was more than three times the experimental activation energy. Therefore, the direct guest-MOF hopping, and MOF-MOF hopping could be excluded in our system. In a superexchange process that indirectly coupled guest molecules with other guest molecules, the energy differences of initial and final $\Delta E_{g,g'} \sim 0 \text{ eV}$ resulted in $E_a \sim \lambda/4$ which was comparable to experimental values. The direct transfer between guest molecules did not depend on ΔE_{gh} and E_a ; it was one order of magnitude smaller than superexchange processes. This difference was due to very small electronic couplings of $J < 10^{-7} \text{ eV}$ between guest molecules for direct hops. If the estimated $\Delta E_{gh} < 0.4 \text{ eV}$, then the electron transfer was mainly from direct guest-MOF-guest process, but the superexchange rate exceeded the rates of any direct process by several orders of magnitude. We concluded that the superexchange process was more plausible than other processes in these systems.

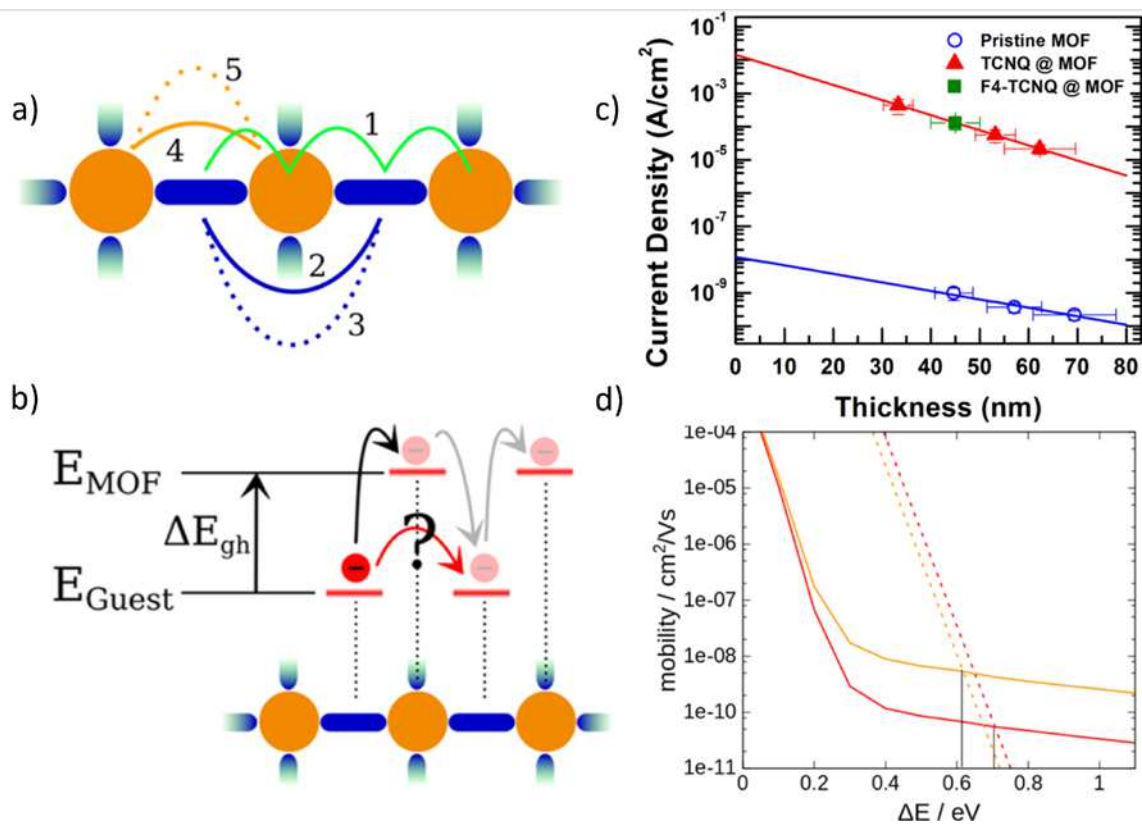


Figure 5. Charge transfer in guest-MOF system via hopping processes. a) Possible first-order transfer processes (solid lines) between guest and MOF sites (1), direct transfer between guest-guest and MOF-MOF sites (2,4), and second-order superexchange processes, dashed lines (3,5). b) Transfer between the LUMO orbitals of the guest molecules can proceed directly or via occupancy of a virtual state in the MOF. c) Current density of pristine MOF (blue open circle), loaded with TCNQ (red solid triangles) and F4-TCNQ (green solid square). d) Mobility derived from experimental data using injection model (dashed lines) and KMC simulation (solid lines) as a function of energy difference between LUMO of the pristine vs SURMOF loaded with TCNQ (red) and F4-TCNQ

(yellow).²⁶ Reprinted with permission from Ref. 26, Copyright 2019 American Chemical Society.

To compare our model with experimental data, we used an injection model where the current density depends on charge carrier concentration, mobility, and injection barrier as:

$$J(V) \sim n\mu e^{\beta\phi} F(V). \quad (3)$$

The electronic transport processes in the MOF loaded with guests (TCNQ, F4-TCNQ) are shown in Fig. 5.

The current density for the pristine and loaded MOF is shown in Fig. 5c), and a direct comparison between derived experimental data using an injection model and KMC simulation based on DFT input is shown in Fig. 5d). The mobility curves show the intersect at 0.6 eV (F4-TCNQ) and 0.71 eV (TCNQ), in agreement with the energy difference of the LUMO level in pristine and loaded HKUST-1 from DFT, ~ 0.6 eV. However, the relative order of LUMOs of the MOF loaded with F4-TCNQ and TCNQ using DFT disagreed with the calculated injection barrier difference of 0.1 eV.

Conclusion

The unprecedented chemical and structural tunability of MOFs through functionalization and various host-guest interactions makes them an ideal platform to design advanced functional materials. Computational tools have been developed that can increasingly aid in the optimization of these materials. Structure building tools, such as AuToGraFS, combined with classical force fields enable fast screening of organic linkers that can help guide experimentalists towards synthesis of MOFs with desirable properties. A good example for such an approach was the screening of linkers to develop bright photoluminescent MOFs and the other applications reviewed here. Multiscale modeling using methods such as Quantum Patch and KMC permit calculation of the conductivity/mobility of pristine and loaded MOFs with reasonable accuracy, usually about one order of magnitude. Overall, there has been a lot of progress in predicting and characterizing MOF structures, especially using electronic structure methods. Despite these advances there remain many challenges with which computational methods still struggle.

The chemical stability of MOFs and their assembly process, which involves chemical reactions and solvent interactions, is controlled by a wide variety of other experimental parameters that are still very difficult to model using computational methods. The calculation of excited state properties remains mostly limited to molecular cluster models (monomer, dimer, trimer, etc.) using TD-DFT and RPA; no fully periodic structures calculations are presently available. One of the drawbacks of TD-DFT is that calculated HOMO-LUMO gaps strongly depend on the chosen exchange-correlation functional. Higher-level methods such as GW+BSE are still very challenging at the scale of typical MOFs due to considerable computational cost. One further remaining challenge is the influence of polycrystallinity in MOFs when comparing the experimental electronic properties to computational results. The effects of grain boundaries and defects such as

missing SBUs or linkers are not considered in many computational studies, which presently mostly model perfect crystal structures. Multiscale modeling that includes grain boundaries and defects may further improve the accuracy of computational methods.

Acknowledgments

Authors acknowledged the Deutsche Forschungsgemeinschaft (DFG, German Research Foundation) under the Germany Excellence Strategy via the Excellence Cluster 3D Matter Made to Order (grant no. EXC-2082/1-390761711) and the European Union Horizon 2020 research and innovation program under grant agreement no. 646176 (EXTMOS)

References

- 1 H. M. El-Kaderi, J. R. Hunt, J. L. Mendoza-Cortés, A. P. Côté, R. E. Taylor, M. O’Keeffe, and O. M. Yaghi, *Science* (80-.),
- 2 Y. Pramudya and J. L. Mendoza-Cortes, *J. Am. Chem. Soc.*, 2016, **138**, 15204–15213.
- 3 R. J. Verploegh, S. Nair and D. S. Sholl, *J. Am. Chem. Soc.*, 2015, **137**, 15760–15771.
- 4 S. Garg, H. Schwartz, M. Kozłowska, A. B. Kanj, K. Müller, W. Wenzel, U. Ruschewitz and L. Heinke, *Angew. Chemie Int. Ed.*, 2019, **58**, 1193–1197.
- 5 X. Liu, M. Kozłowska, T. Okkali, D. Wagner, T. Higashino, G. Brenner-Weiß, S. M. Marschner, Z. Fu, Q. Zhang, H. Imahori, S. Bräse, W. Wenzel, C. Wöll and L. Heinke, *Angew. Chemie Int. Ed.*, 2019, **58**, 9590–9595.
- 6 R. Haldar, A. Mazel, M. Krstić, Q. Zhang, M. Jakoby, I. A. Howard, B. S. Richards, N. Jung, D. Jacquemin, S. Diring, W. Wenzel, F. Odobel and C. Wöll, *Nat. Commun.*, 2019, **10**, 1–7.
- 7 M. A. Addicoat, D. E. Coupry and T. Heine, *J. Phys. Chem. A*, 2014, **118**, 9607–9614.
- 8 D. E. Coupry, M. A. Addicoat and T. Heine, *J. Chem. Theory Comput.*, 2016, **12**, 5215–5225.
- 9 P. G. Boyd, S. M. Moosavi, M. Witman and B. Smit, *J. Phys. Chem. Lett.*, 2017, **8**, 357–363.
- 10 A. K. Rappe, C. J. Casewit, K. S. Colwell, W. A. Goddard and W. M. Skiff, *J. Am. Chem. Soc.*, 1992, **114**, 10024–10035.
- 11 M. Elstner, D. Porezag, G. Jungnickel, J. Elsner, M. Haugk and T. Frauenheim, *Phys. Rev. B - Condens. Matter Mater. Phys.*, 1998, **58**, 7260–7268.
- 12 C. Bannwarth, S. Ehlert and S. Grimme, *J. Chem. Theory Comput.*, 2019, **15**, 1652–1671.
- 13 S. Das, J. E. Coulter and E. Manousakis, *Phys. Rev. B - Condens. Matter Mater. Phys.*, 2015, **91**, 115105.
- 14 J. E. Coulter, E. Manousakis and A. Gali, *Phys. Rev. B - Condens. Matter Mater. Phys.*, 2013, **88**, 041107.
- 15 D. Bohm and D. Pines, *Phys. Rev.*, 1951, **82**, 625–634.
- 16 D. Pines and D. Bohm, *Phys. Rev.*, 1952, **85**, 338–353.
- 17 Y. Pramudya, H. Terletska, S. Pankov, E. Manousakis and V. Dobrosavljević, *Phys.*

Rev. B - Condens. Matter Mater. Phys.

- 18 J. M. Frost, 2017, **96**, 195202.
- 19 V. Stehr, J. Pfister, R. F. Fink, B. Engels and C. Deibel, *Phys. Rev. B - Condens. Matter Mater. Phys.*, 2011, **83**, 155208.
- 20 L. S. Xie, G. Skorupskii and M. Dincă, *Chem. Rev.*, 2020.
- 21 P. Friederich, T. Strunk, W. Wenzel and I. Kondov, in *Procedia Computer Science*, Elsevier B.V., 2016, vol. 80, pp. 1244–1254.
- 22 P. Friederich, F. Symalla, V. Meded, T. Neumann and W. Wenzel, *J. Chem. Theory Comput.*, 2014, **10**, 3720–3725.
- 23 A. Fediai, F. Symalla, P. Friederich and W. Wenzel, *Nat. Commun.*, 2019, **10**, 1–7.
- 24 Z. Zhang, K. Müller, S. Heidrich, M. Koenig, T. Hashem, T. Schlöder, D. Bléger, W. Wenzel and L. Heinke, *J. Phys. Chem. Lett.*, 2019, **10**, 6626–6633.
- 25 M. Adams, M. Kozłowska, N. Baroni, M. Oldenburg, R. Ma, D. Busko, A. Turshatov, G. Emandi, M. O. Senge, R. Haldar, C. Wöll, G. U. Nienhaus, B. S. Richards and I. A. Howard, *ACS Appl. Mater. Interfaces*, 2019, **11**, 15688–15697.
- 26 T. Neumann, J. Liu, T. Wächter, P. Friederich, F. Symalla, A. Welle, V. Mugnaini, V. Meded, M. Zharnikov, C. Wöll and W. Wenzel, *ACS Nano*, 2016, **10**, 7085–7093.
- 27 A. A. Talin, A. Centrone, A. C. Ford, M. E. Foster, V. Stavila, P. Haney, R. A. Kinney, V. Szalai, F. El Gabaly, H. P. Yoon, F. Léonard and M. D. Allendorf, *Science (80-.)*, 2014, **343**, 66–69.

Repository KITopen

Dies ist ein Postprint/begutachtetes Manuskript.

Empfohlene Zitierung:

Pramudya, Y.; Kozłowska, M.; Heidrich, S.; Krstić, M.; Haldar, R.; Neumann, T.; Schlöder, T.; Zhang, Q.; Symalla, F.; Hassan, Z. M.; Liu, X.; Heinke, L.; Wöll, C.; Wenzel, W.

[The Interplay of Conformation and Electronic Structure in Metal Organic Frameworks](#)

2020. ECS transactions, 98

[doi: 10.554/IR/1000127604](https://doi.org/10.554/IR/1000127604)

Zitierung der Originalveröffentlichung:

Pramudya, Y.; Kozłowska, M.; Heidrich, S.; Krstić, M.; Haldar, R.; Neumann, T.; Schlöder, T.; Zhang, Q.; Symalla, F.; Hassan, Z. M.; Liu, X.; Heinke, L.; Wöll, C.; Wenzel, W.

[The Interplay of Conformation and Electronic Structure in Metal Organic Frameworks](#)

2020. ECS transactions, 98 (8), 3–13.

[doi:10.1149/09808.0003ecst](https://doi.org/10.1149/09808.0003ecst)

Lizenzinformationen: [KITopen-Lizenz](#)